A Machine Learning Potential for Hexagonal Boron Nitride Applied to Thermally and Mechanically Induced Rippling

Fabian L. Thiemann[1,2], Patrick Rowe[1], Erich A. Müller[2], and Angelos Michaelides[1]

[1]Thomas Young Centre, London Centre for Nanotechnology, and Department of Physics and Astronomy, University College London, Gower Street, London, WC1E 6BT, United Kingdom
[2]Department of Chemical Engineering, Imperial College London, South Kensington Campus, London SW7 2AZ, United Kingdom

In this supplementary information, we provide additional details on certain aspects of the study reported in the manuscript. These are mainly focused on the performance of the hBN-GAP and the chosen DFT functional. The following issues are discussed:

1 Benchmarking of DFT functionals applied to hBN **S2**

2 Force correlation plots **S5**

3 Interlayer binding curve **S7**

4 Formation energy of nanotubes **S8**

5 Phonon dispersion curves for hBN monolayer **S9**

6 Phonon dispersion curves for bulk hBN **S10**

7 Phonon dispersion curves for a (6,6) nanotube **S12**

8 Benchmarking the efficiency of the hBN-GAP **S14**

9 Impact of box shape and size on the rippling amplitude **S16**

1 Benchmarking of DFT functionals applied to hBN

Given the large diversity of the zoo of DFT functionals, it is not surprising that different established force fields are not fitted to *ab initio* data obtained with the identical functional. In the main document, however, we benchmarked the accuracy of these models exclusively based on the specific functional chosen for the generation of the training set of the hBN-GAP. This analysis is, therefore, slightly biased and we aim to provide a more neutral picture by reporting the performance of different functionals for basic crystalline properties of hBN. We compare our selected functional, PBE [1] with the local dispersion correction D3 [2] using Becke-Johnson damping [3], with two non-local dispersion inclusive functionals, optB86b-vdW [4] and optB88-vdW [5], LDA [6], PBE, and PBE using the local dispersion corrections of Tkatchenko and Scheffler (TS) [7]. Further, we perform all calculations for PBE+D3 with both software packages VASP and QUANTUM ESPRESSO (QE) to verify they yield the same result.

Table S1: Comparison of lattice parameters for the different hBN phases between different DFT exchange-correlation functional and with respect to experimental data.

	Lattice Parameter [Å]				
	Bulk		Monolayer	Nanotube	
	a	c	a	(10,0)	(10,10)
LDA	2.49	6.49	2.49	4.30	2.49
PBE	2.51	8.47	2.51	4.34	2.51
PBE+TS	2.51	6.69	2.51	4.34	2.51
PBE+D3 (VASP)	2.51	6.61	2.51	4.34	2.51
PBE+D3 (QE)	2.51	6.62	2.51	4.34	2.51
optB88-vdW	2.51	6.58	2.51	4.34	2.51
optB86b-vdW	2.51	6.50	2.51	4.34	2.51
Experiment [8]	2.50	6.66	2.50	–	–

In table S1 we show the predictions of the tested functionals for the lattice parameters of bulk and monolayer hBN as well as two nanotubes of different chirality. While the in-plane lattice parameters of layered hBN as well as the nanotubes geometries are almost independent of the functional selected, deviations between functionals are observed for the equilibrium interlayer distance of bulk hBN. The best agreement with experimental measurements [8] is achieved by PBE+TS and PBE+D3. Conversely, PBE without dispersion corrections overestimates the lattice parameter significantly by almost 2 Å. Despite their high similarity, the predictions made by optB88-vdW and optB86b-vdW differ by 0.08 Å. A high agreement for all systems is found between both software packages.

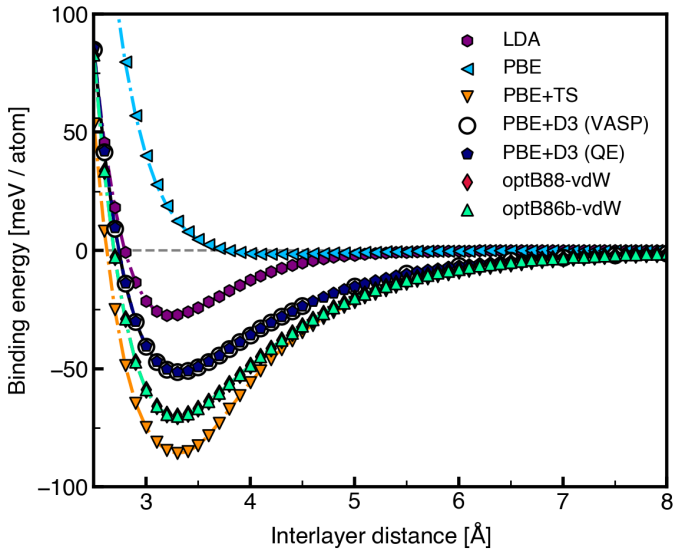

Figure S1: Interlayer interaction curves for bulk hBN predicted by different DFT functionals. The binding energy is computed as function of a varying interlayer distance between sheet in AA′ stacking.

We also computed the binding curve between hBN sheets in the bulk phase as shown in figure S1. The curves for LDA, PBE, and optB88-vdW agree very

well with previous work [9]. Similar applies for the interaction energy predicted by PBE+TS [10]. The binding curves predicted by optB88-vdW and optB86b-vdW are almost identical with the exception of the small shift of the minimum towards a shorter interlayer separation.

Eventually, we calculated the relative stability of the systems analysed in table S1 relative to the bulk phase. The results shown in figure S2 demonstrate once again the high similarity non-local vdW inclusive functionals. The large and small values shown for PBE+TS and PBE are the result of the deep and shallow potential well of the layer interaction curve, respectively.

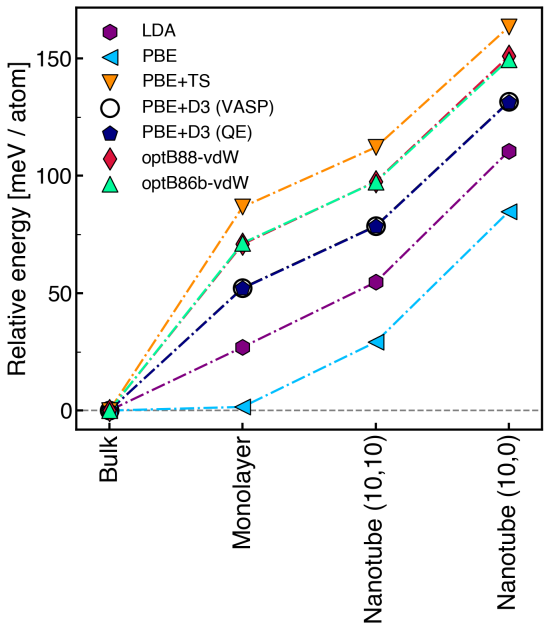

Figure S2: Formation energies of several hBN configurations computed with different DFT functionals. All energies are plotted relative to bulk hBN.

2 Force correlation plots

Despite not being a sufficient criterion to assess the quality of a potential, comparing the average force error for a set of configurations with respect to DFT is a natural and essential metric. We pick 1450 configurations from our previously generated database at random which have not been used in the training process and compute the forces with DFT, the hBN-GAP, and the force fields used in the main text. The structures comprise between 98 and 200 atoms and include 397 single layers of hBN, 551 multilayered and bulk structures, as well as 502 nanotubes of different chiralities. Figure S3 shows the force correlation plots for all potentials tested separately for each structure group and the related RMSE. The hBN-GAP achieves a very high agreement with the DFT forces whereby its RMSE is at least one order of magnitude smaller than that of its existing analogues. This holds throughout all different configurations, despite the good performance of Tersoff and ExTeP particularly for monolayers. All established potentials struggle to make accurate predictions for multilayered hBN. Despite a significantly better performance regarding macroscopic properties, the employed ILP corrections increase the RMSE of the bond-order potentials slightly. The ReaxFF shows high deviations from DFT which might be reduced by using a different parameter set than applied in this work. When changing the DFT functional used as reference to compute the force error, small differences of up to 20 meV/Å were observed.

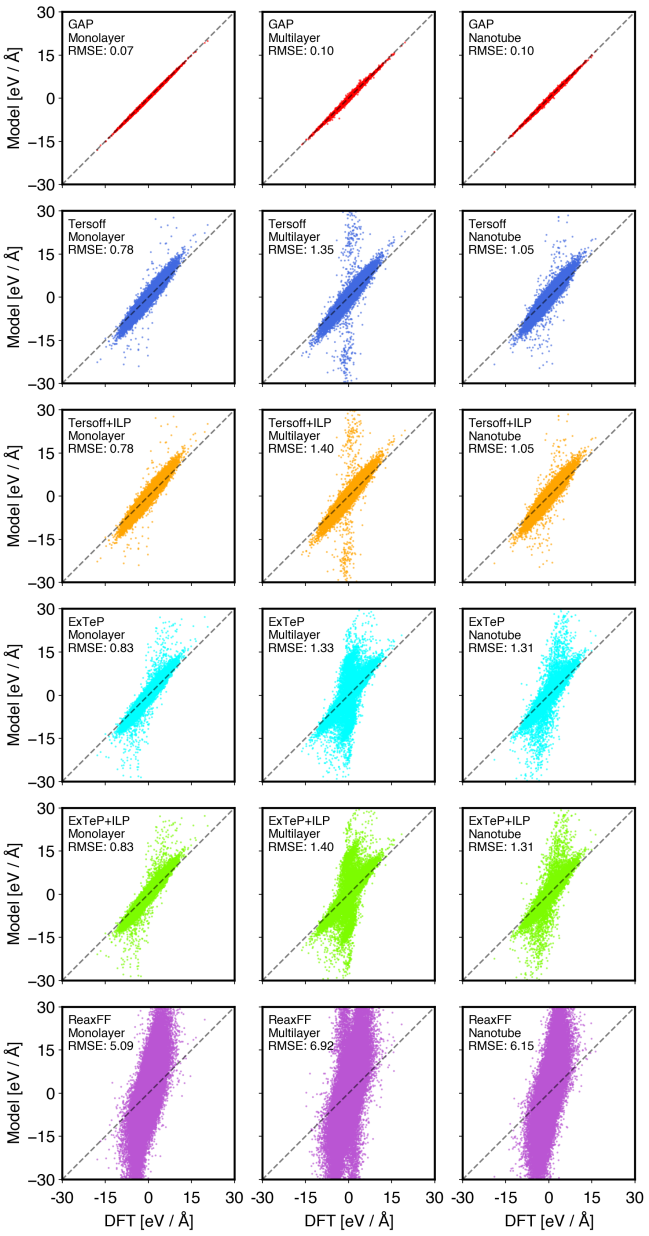

Figure S3: Comparision of atomistic forces predicted by different models with respect to DFT (PBE+D3) for configurations in the validation set including mono and multilayers as well as nanotubes. The RMSE is calculated for each class of structures separately and is given in the units of eV/Å.

3 Interlayer binding curve

As already emphasised above, predicting the binding energy curve of bulk hBN accurately is an essential requirement for appropriately capturing the out-of-plane elastic constant, C_{33}. Here, we report the performance of our hBN-GAP with respect to its DFT reference and in comparison with the established force fields introduced in the main document. We note that Tersoff + ILP and ExTeP + ILP yield the same curve as the interaction is purely modelled by the ILP. From figure S4 it can be seen that the hBN-GAP agrees very well with DFT. The slowly decaying tail is accurately predicted due to the inclusion of a 2B-based model with an extended cut-off of 10 Å. The ILP shows a small overbinding but overall agrees very well with our the reference calculations too. In case of ReaxFF a maximum appears at about 5.5 Å.

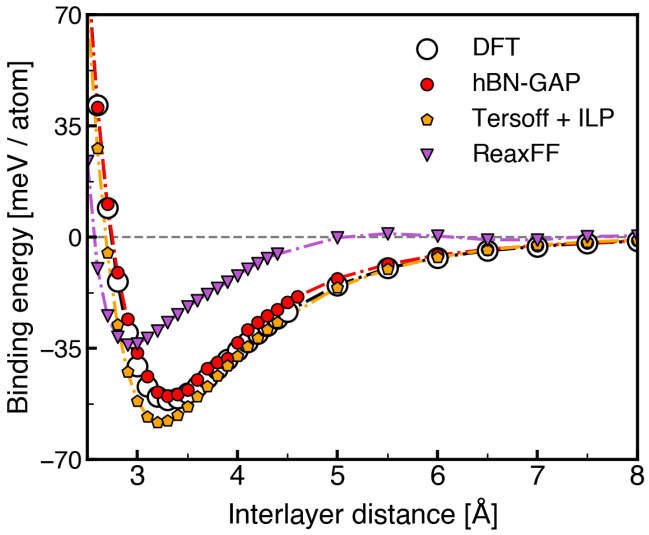

Figure S4: Interlayer interaction curves for bulk hBN predicted the hBN-GAP, the chosen DFT functional (PBE+D3) and two other force fields. The binding energy is computed as function of a varying interlayer distance between sheet in AA′ stacking.

4 Formation energy of nanotubes

In the main text we compute the formation energies of different hBN allotropes including different nanotubes. Here, we extend this analysis to nanotubes of charilities between $4 \leq \mathrm{m}, \mathrm{n} \leq 14$. In contrast to the the previous analysis, here the energies are given relative to a hBN monolayer. Therefore, it is sufficient to compare the agreement of the hBN-GAP with its DFT reference only with respect to the bond-order potentials Tersoff and ExTeP without the ILP extension as well as to the ReaxFF. From figure S5 it can be seen that both the hBN-GAP and the Tersoff potential perform very well while the ExTeP shows some inaccuracies regarding the energy difference between zigzag and armchair nanotubes. From the inset, it can be seen that the ReaxFF suffers from a similar issue although slightly less pronounced.

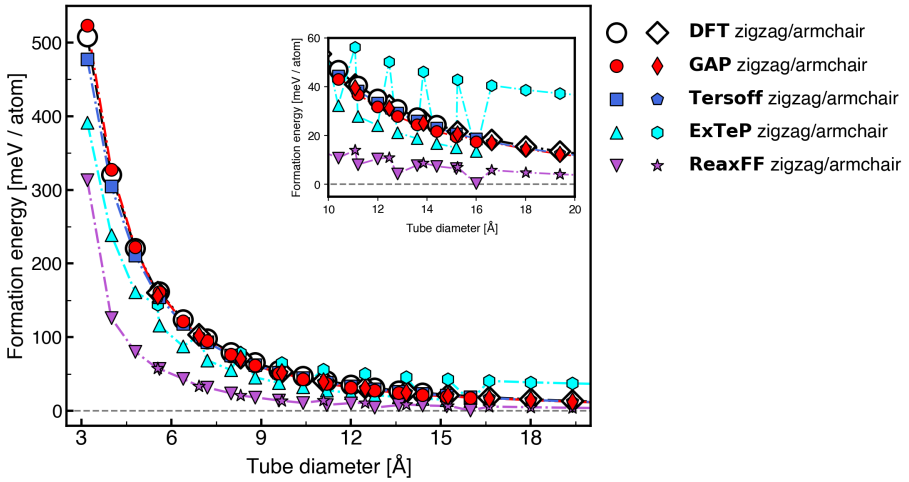

Figure S5: Relative formation energies of nanotubes of armchair and zigzag predicted by DFT (PBE+D3), GAP and existing force fields as function of the tube diameter. A hBN monolayer serves as reference for the formation energies. For the sake of clarity, the ILP extended bond-order potentials are not plotted here as the ILP has no contribution to the potential energy in nanotubes and monolayers.

5 Phonon dispersion curves for hBN monolayer

We report the phonon dispersion curves for a hBN monolayer computed with the established models mentioned in the main text. Similar to the nanotubes discussed above, it is sufficient to evaluate the performance of the bond-order potentials Tersoff and ExTeP without ILP due to absence of a contribution for isolated sheets. The respective dispersion curves are shown in figure S6. While we also computed the phonons with the ReaxFF, no physically reasonable results were obtained. This can be easily explained by the wrong prediction of the equilibrium shape discussed in the main text. This observation is also persistent throughout bulk hBN and nanotubes as well as for applying the parameter set most recently developed for the adsorption of hBN on nickel [11]. Tersoff and ExTeP provide an accurate description for the ZA mode except a small overestimation at K. Both models, however, are not able to reproduce the high-frequency modes, particularly LO and TO, and show high deviations with respect to DFT.

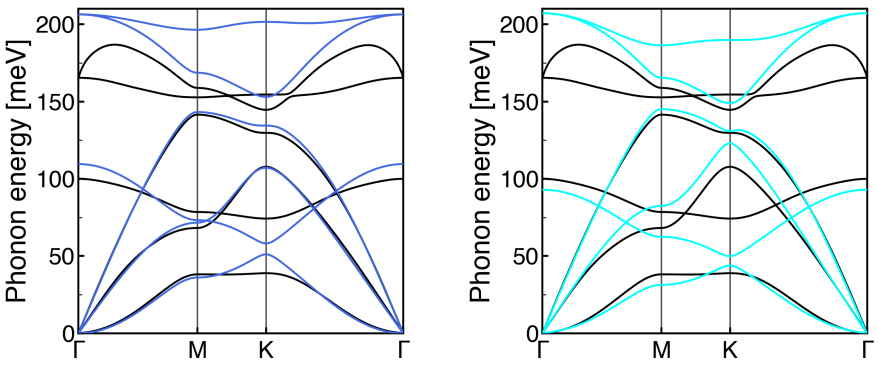

Figure S6: Phonon dispersion curves calculated for monolayer hBN. The black line corresponds to the reference DFT (PBE) calculations while the coloured represents the Tersoff (left) and ExTeP (right) potentials. The computed dispersion curves are identical for their ILP extended analogues.

6 Phonon dispersion curves for bulk hBN

Here, we present the phonons for bulk hBN computed with the hBN-GAP and the established potentials included in the benchmarking. Instead of comparing to DFT calculations, however, we evaluate the models' performance based on experimental measurements. Firstly, because a good agreement between experiment and theoretical prediction is generally of highest priority. Secondly, the the D3 Grimme dispersion correction method is not accessible in QE for DFPT calculations. While this is not a significant problem for monolayer or nanotubes due to the lack of dispersion interactions, it prevents an accurate prediction of the dispersion curve of bulk hBN where vdW interactions between adjacent layers play a key role.

Figure S7 shows the dispersion curves predicted by the hBN-GAP in comparison to experiments [12–15]. For polar bulk materials, the induced macroscopic electric field results in a non-degeneracy of the LO and the transverse optical (TO) modes close to the Γ -point, also known as LO-TO splitting. While this effect is captured by the Raman and infrared measurements, the hBN-GAP fails to reproduce the shift of the LO branch due to the non-explicit treatment of charges. All other all other features of the dispersion curve are very well predicted by hBN with the exception of a small deviation for the acoustic branches between A and Γ.

In contrast to the monolayer, different phonon dispersion curves are obtained by extending Tersoff and ExTep with ILP. As shown in figure S8 exclusively using either Tersoff or ExTeP results in the same spectrum as for the monolayer. Due to the short cutoff of both potentials the sheets are not interacting and, thus, the dispersion curves correspond to those of an isolated hBN sheet for

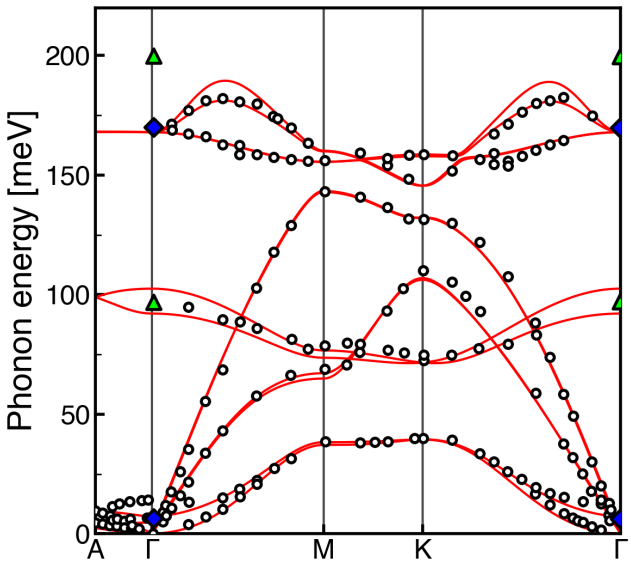

Figure S7: Phonon dispersion curves for bulk hBN predicted by the hBN-GAP compared to experimental measurements using IXR, infrared and Raman spectroscopy. The continuous lines represent the calculated dispersion curves whereas the open black circles corresponds to the IXR measurements [12]. The blue diamonds and green triangles at the Γ-point visualise the Raman [13] and infrared data [13–15].

each sheet which overlap. As expected, applying the ILP correction leads to an improvement particularly for low frequencies between A and Γ. Moreover, a small side-shift of the bands can be observed due to the newly introduced inter-molecular interactions. However, high deviations for the optical modes remain. Due to the lack of explicit charges, no LO-TO splitting can be described with potentials shown in figure S8.

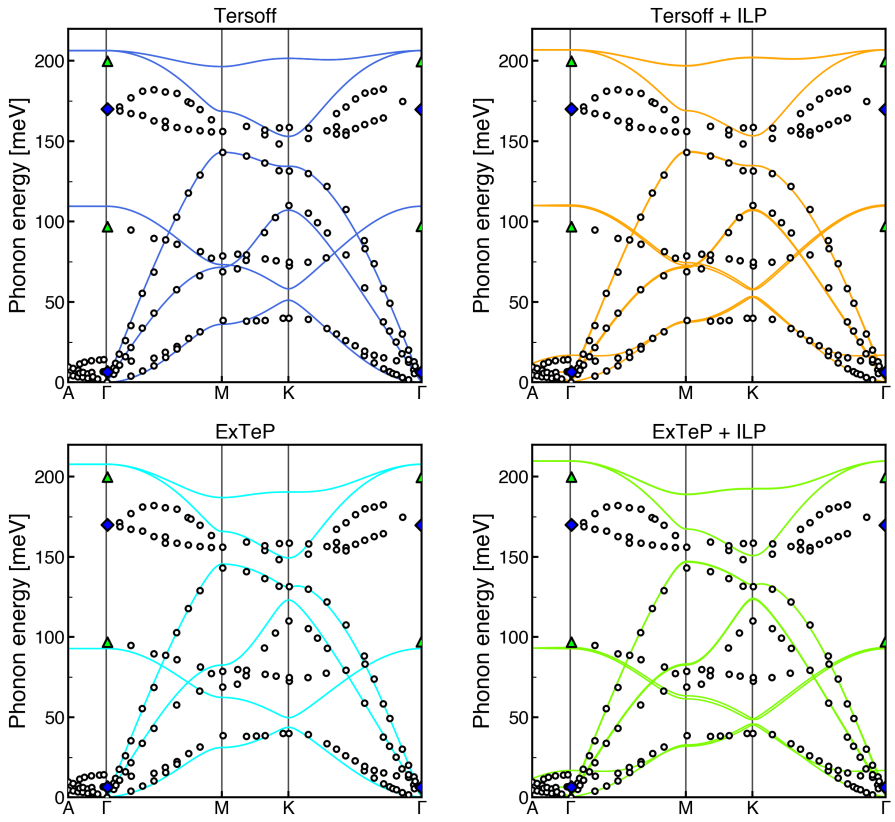

Figure S8: Phonon dispersion curves for bulk hBN predicted by the established potentials discussed in the manuscript compared to experimental measurements using IXR, infrared and Raman spectroscopy. The continuous lines represent the calculated dispersion curves whereas the open black circles corresponds to the IXR measurements [12]. The blue diamonds and green triangles at the Γ-point visualise the Raman [13] and infrared data [13–15].

7 Phonon dispersion curves for a (6,6) nanotube

In figure S9 we show the phonon dispersion curve for a hBN (6,6) nanotube computed with the Tersoff and ExTeP as well as their agreement with DFT. Due to the large number of bands, the absolute deviation of the density of states (DOS) serves a appropriate metric to evaluate models. Analogously to the phonons predicted for the hBN allotropes above, both potentials can not

capture the high frequency modes accurately. The bundle of flat bands which is located at about 150 meV according to DFT is predicted to be at a frequency of 40 to 50 meV above in both cases.

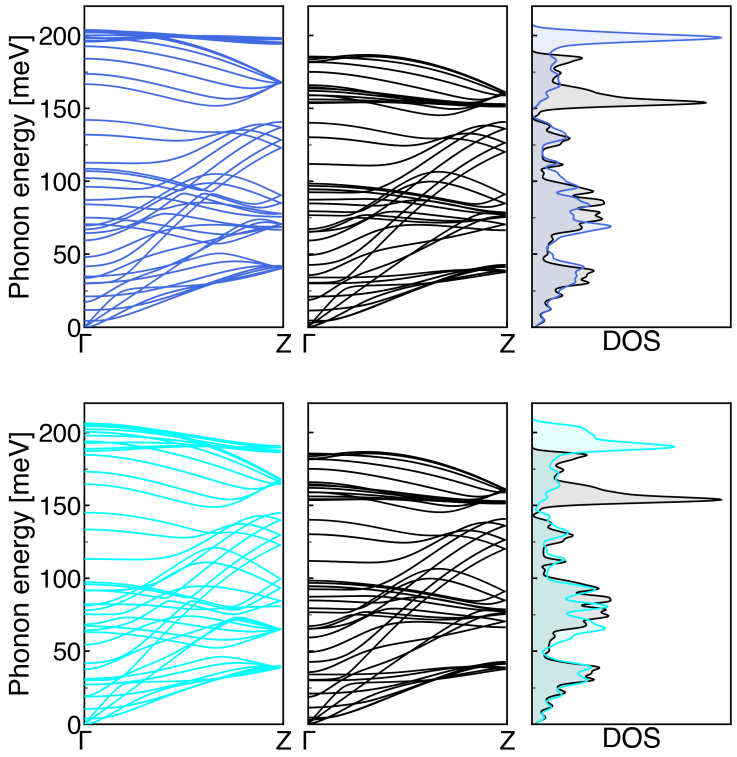

Figure S9: Phonon dispersion curves calculated a (6,6) hBN nanotube predicted by the Tersoff (top) and ExTeP potential (bottom). The black line corresponds to the reference DFT (PBE) calculations while the coloured lines represent the different established models. The DOS is calculated for both methods and plotted against the DFT result on the right hand side.

8 Benchmarking the efficiency of the hBN-GAP

So far, we were mainly concerned with evaluating the accuracy of the hBN-GAP and have not focused on the efficiency advantages with respect to DFT. However, the significantly reduced computational costs are the key benefit of choosing the hBN-GAP over DFT. In order to quantify the saved resources we benchmark the efficiency of our newly introduced model by performing MD simulations and compare the costs to AIMD performed in VASP and to the Tersoff potential. As we expect a similar performance for all force fields discussed, including one of them in this evaluation seems sufficient for our purposes.

Our system of choice for this benchmarking study is a orthorombic shaped hBN monolayer with periodic boundary conditions. We add 15 Å of vacuum in z-direction to minimise the interaction between periodic images in DFT. The system size varies between 8 and 12800 atoms and simulations are conducted in the NVT ensemble at 1000 K. The electronic structure setup is identical to the one used for the generation of training data except a looser convergence criterion of 10^{-4} eV and that all calculations are done at the gamma point. All AIMD simulations are started with pre-converged wavefunctions to reduce the number of required electronic convergence cyclce at the first timestep. Trajectories of 20000 timesteps are generated for hBN-GAP and Tersoff. For the VASP AIMD simulations we compute a trajectory of 10 timesteps. All simulations are performed on the Thomas cluster, the UK National Tier 2 High Performance Computing Hub for Materials and Molecular Modelling. While for AIMD simulations 72 cores spread over three nodes are used, all simulations with hBN-GAP and Tersoff are done on one node only to minimise the communication time between nodes for very small system sizes. All measured simulations times are normalised with the number of steps and number of cores used.

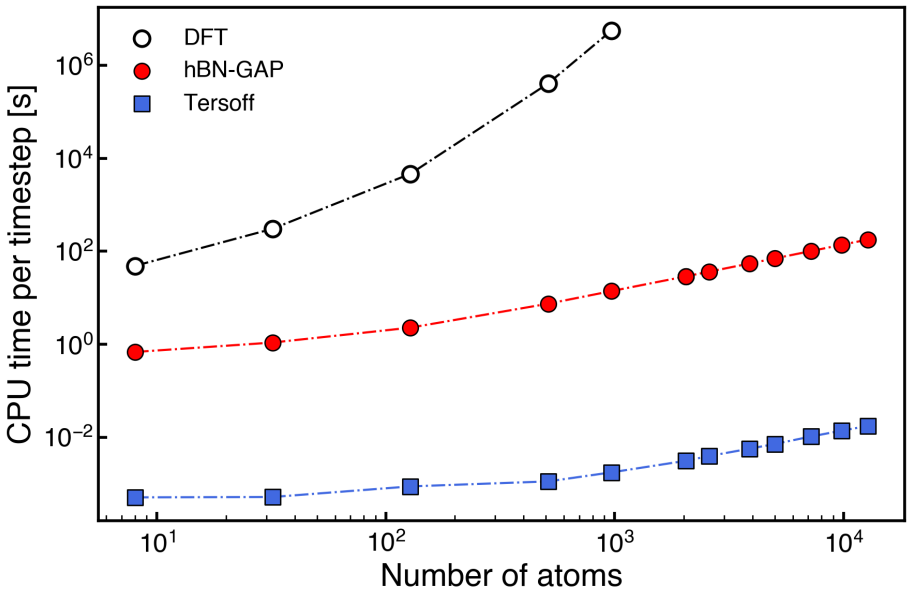

Figure S10: Computational costs of the hBN-GAP in comparison with DFT (PBE+D3) and the Tersoff potential as function of system size. The CPU time per timestep is normalised with respect to the number of processors used.

Figure S10 shows the computational costs spent per timestep for the different models and system sizes. Clearly, the hBN-GAP is several orders of magnitude cheaper than DFT. This becomes more pronounced as we increase the number of atoms. While both the hBN-GAP and the Tersoff potential scale roughly with $N \log N$, whereby N is the number of atoms, DFT scales cubically with number of electrons making it unfeasible for large systems. This is also emphasised by the missing data for DFT above 2048 atoms in figure S10. It was not possible to perform 10 timesteps of AIMD with the computational and electronic setup chosen for the larger systems considered in this study.

9 Impact of box shape and size on the rippling amplitude

To investigate the impact of the shape of the simulation box on the average rippling amplitude we perform GAP MD for monoclinic and orthorombic cells of hBN and graphene with varying size between 1800 and 10952 atoms. Both in-plane lattice vectors of the monoclinic box are of length L while the measures of the orthorombic box are $L \times \frac{\sqrt{3}}{2}L$, whereby L changes according to material and system size. As we are mainly interested in the capabilities of the developed hBN-GAP to predict coherently moving ripples all systems analysed are exposed to -1.0 % strain based on their equilibrium lattice parameter at 300 K. We use the same simulation settings as described in the main document. All systems are equilibrated for at least 50 ps before the maximum out-of-plane displacement is measured and averaged for a sampling time ranging from 150 to 400 ps.

Figure S11 summarises the findings of this analysis. The difference in the box shapes is reflected in distinct rippling patterns as shown in part B and C. While the compression of the orthorombic cell results in a meander-shaped soliton propagating through the sheet, triangularly formed ripples are observed in the monoclinic simulation box. In part C of figure S11 we report the averaged amplitude of the ripples as function of the minimum box length L_0 which corresponds to L and $\frac{\sqrt{3}}{2}L$ for monoclinic and orthorombic boxes, respectively. The difference in the box length between graphene and hBN systems with identical box shape and number of atoms is induced by the smaller lattice parameter of graphene. Irrespective of the taken shape of the ripples, an almost linear trend is observed for the rippling amplitude with respect to the system size. This

holds true for both materials hBN and graphene which justifies the comparative analysis based on the same box shape and system size.

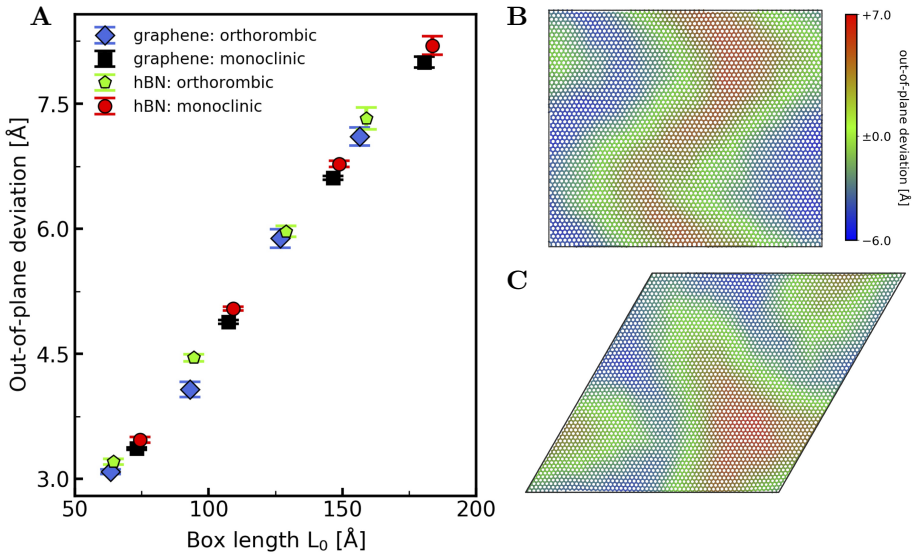

Figure S11: Analysis of the box shape and size dependence of the rippling pattern and amplitude. (**A**): Average rippling amplitude as function of the minimum box length L_0. For monoclinic boxes L_0 is equal to the length L of the lattice vectors while in case of orthocombic cells it corresponds to the lattice vector with minimum length of $\sqrt{3}/2$L. (**B**): Snapshot of the GAP-MD trajectory of an isolated sheet of hBN in a orthorombic box with 7200 atoms. The atoms are coloured according to their out-of-plane displacement. (**C**): Snapshot of the GAP-MD trajectory of an isolated sheet of hBN in a monoclinic box with 7200 atoms. Atoms are identically colour coded as in case of the orthorombic box.

References

[1] J. P. Perdew, K. Burke, and M. Ernzerhof, "Generalized gradient approximation made simple," *Physical Review Letters*, vol. 77, no. 18, pp. 3865–3868, 1996.

[2] S. Grimme, J. Antony, S. Ehrlich, and H. Krieg, "A consistent and accurate ab initio parametrization of density functional dispersion correction (DFT-D) for the 94 elements H-Pu," *Journal of Chemical Physics*, vol. 132, no. 15, 2010.

[3] S. Grimme, S. Ehrlich, and L. Goerigk, "Effect of the Damping Function in Dispersion Corrected Density Functional Theory," *Journal of Computational Chemistry*, vol. 32, p. 1456, 2011.

[4] J. Klimeš, D. R. Bowler, and A. Michaelides, "Van der Waals density functionals applied to solids," *Physical Review B - Condensed Matter and Materials Physics*, vol. 83, no. 19, pp. 1–13, 2011.

[5] J. Klimeš, D. R. Bowler, and A. Michaelides, "Chemical accuracy for the van der Waals density functional," *Journal of Physics Condensed Matter*, vol. 22, p. 022201, 2010.

[6] D. M. Ceperley and B. J. Alder, "Ground State of the Electron Gas by a Stochastic Method," *Physical Review Letters*, vol. 45, no. 7, pp. 566–569, 1980.

[7] A. Tkatchenko and M. Scheffler, "Accurate molecular van der Waals interactions from ground-state electron density and free-atom reference data," *Physical Review Letters*, vol. 102, no. 7, pp. 6–9, 2009.

[8] V. L. Solozhenko, G. Will, and F. Elf, "Isothermal compression of hexagonal

graphite-like boron nitride up to 12 GPa," *Solid State Communications*, vol. 96, no. 1, pp. 1–3, 1995.

[9] G. Graziano, J. Klimeš, F. Fernandez-Alonso, and A. Michaelides, "Improved description of soft layered materials with van der Waals density functional theory," *Journal of Physics: Condensed Matter*, vol. 24, p. 424216, 2012.

[10] N. Marom, J. Bernstein, J. Garel, A. Tkatchenko, E. Joselevich, L. Kronik, and O. Hod, "Stacking and registry effects in layered materials: The case of hexagonal boron nitride," *Physical Review Letters*, vol. 105, no. 4, pp. 1–4, 2010.

[11] S. Liu, A. C. Van Duin, D. M. Van Duin, B. Liu, and J. H. Edgar, "Atomistic Insights into Nucleation and Formation of Hexagonal Boron Nitride on Nickel from First-Principles-Based Reactive Molecular Dynamics Simulations," *ACS Nano*, vol. 11, no. 4, pp. 3585–3596, 2017.

[12] J. Serrano, A. Bosak, R. Arenal, M. Krisch, K. Watanabe, T. Taniguchi, H. Kanda, A. Rubio, and L. Wirtz, "Vibrational Properties of Hexagonal Boron Nitride : Inelastic X-Ray Scattering and Ab Initio Calculations," *Physical Review Letters*, vol. 98, p. 095503, 2007.

[13] R. Geick, C. H. Perry, and G. Rupprecht, "Normal modes in hexagonal boron nitride," *Physical Review*, vol. 146, no. 2, pp. 543–547, 1966.

[14] R. J. Nemanich, S. A. Solin, and R. M. Martin, "Light scattering study of boron nitride microcrystals," *Physical Review B*, vol. 23, no. 12, pp. 6348–6356, 1981.

[15] S. Reich, A. C. Ferrari, R. Arenal, A. Loiseau, I. Bello, and J. Robertson, "Resonant Raman scattering in cubic and hexagonal boron nitride," *Physi-*

cal Review B - Condensed Matter and Materials Physics, vol. 71, p. 205201, 2005.